Raman spectra of $CuInSe_2$

H. Tanino
Electrotechnical Laboratory, 1-1-4 Umezono, Tsukuba, Ibaraki 305, Japan

T. Maeda, H. Fujikake, and H. Nakanishi
Faculty of Science and Engineering, Science University of Tokyo, 2641 Yamazaki, Noda, Chiba 278, Japan

S. Endo and T. Irie
Faculty of Engineering, Science University of Tokyo, 1-3 Kagurazaka, Shinjuku, Tokyo 162, Japan
(Received 31 October 1991)

We have measured Raman spectra of $CuInSe_2$ single crystals at room and low temperatures. We have determined all Raman-active modes. The results are in good agreement with the infrared results, but are inconsistent with a previous report of the Raman spectra [J. N. Gan *et al.*, Phys. Rev. B **13**, 3610 (1976)]. The effective charges are estimated from the longitudinal-transverse splitting of the optical-phonon modes. The temperature and pressure dependences of the Γ_1 mode are also presented.

I. INTRODUCTION

The chalcopyrite-type ternary semiconductor $CuInSe_2$ has attracted much attention as a promising material for high-efficiency thin-film solar cells. Raman scattering can sometimes be effective by used to characterize $CuInSe_2$ thin films, which often include different phases or compounds. In 1976, Gan *et al.*[1] reported the Raman spectra of $CuInSe_2$ and performed the mode assignments, but their result was inconsistent with existing infrared spectra.[2–5] Neumann claimed the resemblance between their spectra and the Raman spectra of $CuGaSe_2$.[3,4] Recent reports on thin films are also inconsistent with their spectra.[6–10] Hence, the correspondence between the Raman spectra and the lattice dynamics of $CuInSe_2$ remains unclear.

In this work, we report an extensive study of the polarized Raman spectra of single crystals of $CuInSe_2$ at room and low temperatures. Preliminary results have been presented elsewhere.[11] The temperature and pressure dependences of the Γ_1 mode are also presented.

II. SYSTEMATICS OF $A^{I}B^{III}C_2^{VI}$ CHALCOPYRITE COMPOUNDS AND $CuInSe_2$

From the simplest viewpoint, $CuInSe_2$ is the ternary ($A^{I}B^{III}C_2^{VI}$) analog of the fictitious cubic (pseudobinary II-VI) semiconductor $Zn_{0.5}Cd_{0.5}Se$. This fact is well known[12,13] and simple structural relations between the chalcopyrite-structure compounds and the more familiar zinc-blende (ZB) -structure cubic semiconductor compounds are discussed. In the particular case of $CuInSe_2$, every fictitious $Zn_{0.5}Cd_{0.5}$ cation has been replaced, alternatively along the c direction, by one lighter A^{I} (copper) and one heavier B^{III} (indium) species to form the "Cu-Se"-like and "In-Se"-like bonds. If the replacing species are exchanged, i.e., the cation is replaced by one heavier A^{I} (silver) and one lighter B^{III} (gallium) species, we get another analog chalcopyrite $AgGaSe_2$. Recently, the infrared and Raman spectra of $AgGaSe_2$ has been investigated extensively, and its lattice dynamics has been clarified in detail.[14,15]

The mixing of two cationic species causes a change of space group from T_d^2 ($F\bar{4}3m$) of the ZB-structure compounds to the tetragonal space group D_{2d}^{12} ($I\bar{4}2d$). The long dimension c must be twice the cubic length a for the fictitious and unrelaxed chalcopyrite-structure crystals. However, for real ternary compounds, there is a structural modification represented by the parameter η ($=c/2a$). For $CuInSe_2$, $a=0.5784(1)$ nm, $c=1.1616(5)$ nm, and $\eta=1.004$,[16] which is very close to 1 among all chalcopyrite-structure compounds. Another structural modification is the so-called tetrahedral distortion, which is represented by a single parameter u. Anions C are distorted from the ideal ZB position to make differences between the two types of first-nearest-neighbor distances d_{AC} and d_{BC}. There is a relation that $u=\frac{1}{4}+(d_{AC}^2-d_{BC}^2)/a^2$. For $CuInSe_2$, $d_{AC}=0.242$ nm, $d_{BC}=0.260$ nm, and $u=0.224$.[16] For the above-mentioned analog compound $AgGaSe_2$, $\eta=0.896$ and $u=0.27$,[14] which indicate the much larger modifications than for $CuInSe_2$.

There is a four-to-one relationship between the Brillouin zone (BZ) of the unrelaxed ($\eta=1$ and $u=0.25$) chalcopyrite-structure compounds and the BZ of the corresponding ZB-structure materials, because of the two types of cations and because the volume of the unit cell is four times larger than of ZB materials. Thus, all points $X((0,0,2\pi/a))$, $W((2\pi/a,0,\pi/a))$, and $W((0,2\pi/a,\pi/a))$ of the ZB-structure materials are folded to the central point Γ of the BZ of the chalcopyrite-structure compounds. For better understanding, they are often labeled by $\Gamma[X]$ and $\Gamma[W]$, and distinguished from $\Gamma[\Gamma]$, which is the central point (Brillouin-zone center) for both materials. We use these

notations through this paper.

Since the chalcopyrite-structure compounds have two formula units, i.e., eight atoms per unit cell, which constitute eight sublattices in the crystal, we expect 24 vibrational eigenmodes. They are classified into three groups, i.e., six modes of $\Gamma[\Gamma]$, six modes of $\Gamma[X]$, and 12 modes of $\Gamma[W]$. All $\Gamma[\Gamma]$ modes originate from the Γ_{15} optical mode of the ZB-structure materials. At the Γ point of the chalcopyrite-structure compounds, the 21 optical modes and the three acoustic modes are represented by $1\Gamma_1+2\Gamma_2+3\Gamma_3+3\Gamma_4+6\Gamma_5$ and $1\Gamma_4+1\Gamma_5$, respectively, where only Γ_5 modes are doubly degenerated. The optical modes consist of

$$\Gamma_4^{(7)}[\Gamma_{15}]+\Gamma_5^{(10,16)}[\Gamma_{15}] ,$$

$$\Gamma_2^{(3)}[X_1]+\Gamma_3^{(4)}[X_3]+\Gamma_5^{(11,17)}[X_{5l}]+\Gamma_5^{(12,18)}[X_{5u}] ,$$

and

$$\Gamma_1^{(1)}[W_1]+\Gamma_2^{(2)}[W_1]+\Gamma_3^{(5)}[W_{2l}]+\Gamma_3^{(6)}[W_{2u}]+\Gamma_4^{(8)}[W_{2l}]+\Gamma_4^{(9)}[W_{2u}]+\Gamma_5^{(14,20)}[W_{4l}]+\Gamma_5^{(13,19)}[W_3]+\Gamma_5^{(15,21)}[W_{4u}] ,$$

where the symbols l (lower mode) and u (upper mode) in the subscripts are added to distinguish the modes with the same representations. We can distinguish all the optical modes without the superscript numbers, but we added them for convenience. These superscripts have been taken from the numbers defined by Holah, Webb, and Montgomery.[17] Symmetry coordinates of all optical zone-center modes are listed in Table I.

The relative ordering of the optical modes must be considered by referring to the dispersion curve of the phonon branches in the related ZB-structure materials. Figure 1 summarizes the relationship between the chalcopyrite phonon modes and the phonon branches of the ZB-structure materials. Unfortunately, very little things are known for the W points of all ZB-structure materials. No reports are for ZnSe and CdSe and one experiment of inelastic neutron scattering is for the typical III-V compound GaAs.[18] The phonon branches are schematically drawn in Fig. 1. We can classify the $4\Gamma[X]$ and $9\Gamma[W]$ modes of the chalcopyrite-structure compounds into four groups which originate from transverse acoustic (TA), longitudinal acoustic (LA), longitudinal optical (LO), and transverse optical (TO) branches of the ZB materials, from lower frequencies to higher frequencies. The modes originated from the X_5, W_2 and W_4 points of the TA branch are

$$\Gamma_5^{(11,17)}[X_{5l}]+\Gamma_3^{(5)}[W_{2l}]+\Gamma_4^{(8)}[W_{2l}]+\Gamma_5^{(14,20)}[W_{4l}] ,$$

the modes from the X_3 and W_3 points of the LA branch are

$$\Gamma_3^{(4)}[X_3]+\Gamma_5^{(13,19)}[W_3] ,$$

the modes from the X_1 and W_1 points of the TO branch are

$$\Gamma_2^{(3)}[X_1]+\Gamma_1^{(1)}[W_1]+\Gamma_2^{(2)}[W_1] ,$$

and the modes from the X_5, W_2, and W_4 of the LO branch are

TABLE I. Symmetry coordinates of the 21 optical zone-center phonon modes in $CuInSe_2$. Atomic positions are given by $A^{I}(1)(0,0,0)$, $A^{I}(2)(0,\frac{1}{2},\frac{1}{4})$, $B^{III}(1)(0,0,-\frac{1}{2})$, $B^{III}(2)(0,\frac{1}{2},-\frac{1}{4})$, $C^{VI}(1)(-\frac{1}{4},x,-\frac{1}{8})$, $C^{VI}(2)(\frac{1}{4},-x,-\frac{1}{8})$, $C^{VI}(3)(-x,-\frac{1}{4},\frac{1}{8})$, and $C^{VI}(4)(x,\frac{1}{4},\frac{1}{8})$.

	A^{I} (Cu)	B^{III} (In)	C^{VI} (Se)
$\Gamma_1^{(1)}[W_1]$	0	0	$+y_1-y_2-x_3+x_4$
$\Gamma_2^{(2)}[W_1]$	0	0	$+x_1-x_2+y_3-y_4$
$\Gamma_2^{(3)}[X_1]$	0	0	$+z_1+z_2-z_3-z_4$
$\Gamma_3^{(4)}[X_3]$	$+z_1-z_2$	$+z_1-z_2$	0
$\Gamma_3^{(5)}[W_{2l}]$	$+z_1-z_2$	$-z_1+z_2$	$-y_1+y_2-x_3+x_4$
$\Gamma_3^{(6)}[W_{2u}]$	$+z_1-z_2$	$-z_1+z_2$	$+y_1-y_2+x_3-x_4$
$\Gamma_4^{(7)}[\Gamma_{15}]$	$+z_1+z_2$	$+z_1+z_2$	$-z_1-z_2-z_3-z_4$
$\Gamma_4^{(8)}[W_{2l}]$	$+z_1+z_2$	$-z_1-z_2$	$+x_1-x_2-y_3+y_4$
$\Gamma_4^{(9)}[W_{2u}]$	$+z_1+z_2$	$-z_1-z_2$	$-x_1+x_2+y_3-y_4$
$\Gamma_5^{(10)}[\Gamma_{15}]$	$+x_1+x_2$	$+x_1+x_2$	$-x_1-x_2-x_3-x_4$
$\Gamma_5^{(11)}[X_{5l}]$	$+y_1-y_2$	$+y_1-y_2$	$-x_1-x_2+x_3+x_4$
$\Gamma_5^{(12)}[X_{5u}]$	$+y_1-y_2$	$+y_1-y_2$	$+x_1+x_2-x_3-x_4$
$\Gamma_5^{(13)}[W_3]$	$+x_1+y_1+x_2-y_2$	$-x_1-y_1-x_2+y_2$	0
$\Gamma_5^{(14)}[W_{4l}]$	$+x_1-y_1+x_2+y_2$	$-x_1+y_1-x_2-y_2$	$+z_1-z_2$
$\Gamma_5^{(15)}[W_{4u}]$	$+x_1-y_1+x_2+y_2$	$-x_1+y_1-x_2-y_2$	$-z_1+z_2$
$\Gamma_5^{(16)}[\Gamma_{15}]$	$+y_1+y_2$	$+y_1+y_2$	$-y_1-y_2-y_3-y_4$
$\Gamma_5^{(17)}[X_{5l}]$	$-x_1+x_2$	$-x_1+x_2$	$+y_1+y_2-y_3-y_4$
$\Gamma_5^{(18)}[X_{5u}]$	$-x_1+x_2$	$-x_1+x_2$	$-y_1-y_2+y_3+y_4$
$\Gamma_5^{(19)}[W_3]$	$-x_1+y_1+x_2+y_2$	$+x_1-y_1-x_2-y_2$	0
$\Gamma_5^{(20)}[W_{4l}]$	$+x_1+y_1-x_2+y_2$	$-x_1-y_1+x_2-y_2$	$-z_3+z_4$
$\Gamma_5^{(21)}[W_{4u}]$	$+x_1+y_1-x_2+y_2$	$-x_1-y_1+x_2-y_2$	$+z_3-z_4$

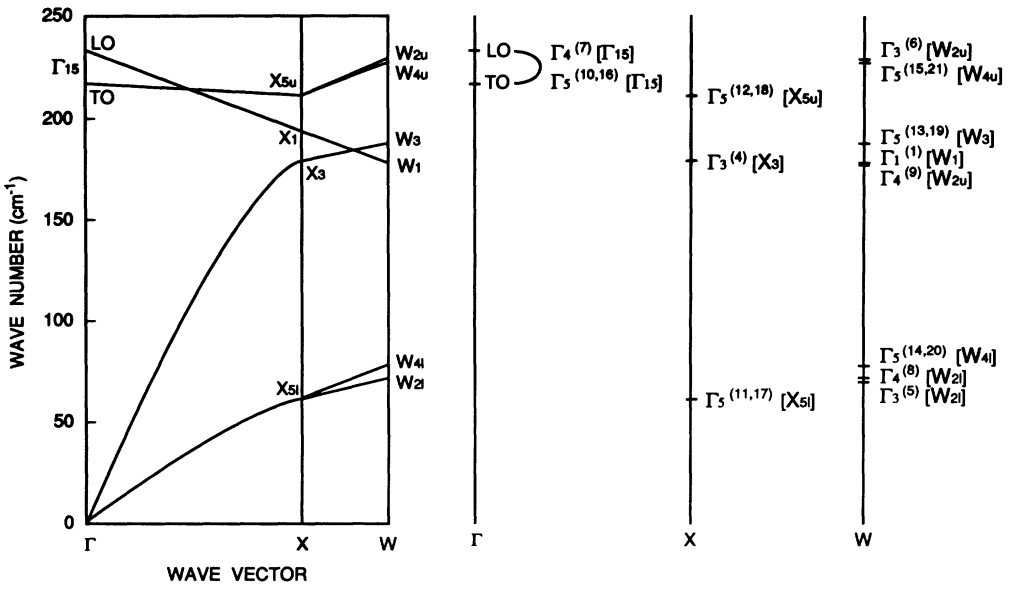

FIG. 1. Schematic drawing to show the relationship between the dispersion curve of the phonon branches in the related zinc-blende-structure (ZB) materials and the chalcopyrite zone-center phonon modes. The energy ordering of the phonon modes is given by our present experimental results.

$\Gamma_5^{(12,18)}[X_{5u}]+\Gamma_3^{(6)}[W_{2u}]+\Gamma_4^{(9)}[W_{2u}]+\Gamma_5^{(15,21)}[W_{4u}]$.

The bending of the dispersion curve in the X-W direction of the ZB-structure materials shows the upshift from X_5 to W_2 and W_4 for the TA and TO branches, and the downshift from X_3 to W_3 for the LA branch and from X_1 to W_1 for the LO branch, respectively. The W_2 point would be always lower than the W_4 point. In summary, we expect the ordering of all optical modes is as follows:

$$\Gamma_5^{(11,17)}[X_{5l}]<\Gamma_3^{(5)}[W_{2l}] ,$$

$$\Gamma_4^{(8)}[W_{2l}]<\Gamma_5^{(14,20)}[W_{4l}]<\Gamma_5^{(13,19)}[W_3]<\Gamma_3^{(4)}[X_3]<\Gamma_1^{(1)}[W_1] ,$$

$$\Gamma_2^{(2)}[W_1]<\Gamma_2^{(3)}[X_1]<\Gamma_5^{(12,18)}[X_{5u}]<\Gamma_3^{(6)}[W_{2u}] ,$$

$$\Gamma_4^{(9)}[W_{2u}]<\Gamma_5^{(15,21)}[W_{4u}]<\Gamma_4^{(7)}[\Gamma_{15}] , \quad \Gamma_5^{(10,16)}[\Gamma_{15}] .$$

We note that the silent modes $\Gamma_2^{(2)}[W_1]$ and $\Gamma_2^{(3)}[X_1]$ will not be discussed in this work. Seeing the Raman-active modes, the experimental results, which will be shown later, do not reproduce perfectly the simple schematic ones. Especially the modes from the LA, LO, and TO branches are mixed variously and exchange the ordering.

In addition, the long-range electrostatic interaction causes the splitting of the longitudinal optical (LO) and transverse optical (TO) frequencies for the Γ_4 and Γ_5 optical modes ($3\Gamma_4+6\Gamma_5$). Since only the Γ_2 modes are silent, we expect that the 22 optical modes $1\Gamma_1+3\Gamma_3+3\Gamma_4(\mathrm{LO})+3\Gamma_4(\mathrm{TO})+6\Gamma_5(\mathrm{LO})+6\Gamma_5(\mathrm{TO})$ are Raman active experimentally.

Infrared-absorption experiments are reported, and some modes have been assigned.[2-4] Though the exact frequencies differ somewhat between the papers, the results are mostly consistent with each other. However, the frequencies of the $\Gamma_4^{(7)}[\Gamma_{15}]$ and $\Gamma_5^{(10,16)}[\Gamma_{15}]$ modes are quite different from those of the previous Raman spectra by Gan *et al.*[1]

In the present work, we have reinvestigated in detail the Raman spectra of $CuInSe_2$. All Raman-active modes have been identified by the low-temperature experiments. The result supports the infrared results, but contradicts the previous Raman result completely.

III. EXPERIMENTAL PROCEDURES

All crystals used in these experiments were grown by melting the elements in an evacuated quartz tube followed by directional freezing. The melted samples are kept at 1020 °C for 48 h, and then slowly cooled down to 500 °C at the rate of −0.1 °C/min. The whole growing process takes about one week. Usually natural surfaces of the samples are the (112) plane, which corresponds to the (111) of the related ZB-structure materials. The principal axes of a or c can be imagined from the triangular slip lines at the surface, even though we cannot distinguish the c axis among the three candidates. We determined the a and c axes by the Burgers precession method. Then we cut and polished the samples to get three faces (100), (110), and (001), which are necessary for the mode assignment by Raman experiments.

The Raman scattering experiments were always performed in a backscattering configuration on the three faces. Table II summarizes the 16 polarization configurations on the three faces used in the present work. The room-temperature experiments were done in Ar atmosphere, and the closed-cycle helium refrigerator

TABLE II. The 16 polarization configurations and the selection rules in the backscattering geometry for the three faces used in the present experiment. We define $X'=(110)$ and $Y'=(1\bar{1}0)$.

Face	Geometry	Allowed symmetry type
(100)	$X(Y,Y)\bar{X}$	$\Gamma_1+\Gamma_3$
	$X(Y,Z)\bar{X}, X(Z,Y)\bar{X}$	Γ_5(LO)
	$X(Z,Z)\bar{X}$	Γ_1
(001)	$Z(X,X)\bar{Z}, Z(Y,Y)\bar{Z}$	$\Gamma_1+\Gamma_3$
	$Z(X,Y)\bar{Z}, Z(Y,X)\bar{Z}$	Γ_4(LO)
	$Z(X',X')\bar{Z}$	$\Gamma_1+\Gamma_4$(LO)
	$Z(X',Y')\bar{Z}, Z(Y',X')\bar{Z}$	Γ_3
	$Z(Y',Y')\bar{Z}$	$\Gamma_1+\Gamma_4$(LO)
(110)	$X'(Y',Y')\bar{X}'$	$\Gamma_1+\Gamma_4$(TO)
	$X'(Y',Z)\bar{X}', X'(Z,Y')\bar{X}'$	Γ_5(TO)
	$X'(Z,Z)\bar{X}'$	Γ_1

was used with the samples in vacuum for the low-temperature experiments. The Ar^+ ion laser at 2.41 eV was used as a light source. The Raman spectrometer consists of a position-sensitive photomultiplier ITT F4146M and a triple-stage spectrograph DILOR XY with a stigmatic optical correction.[19] The spectrometer slit width was set to 100 μm, leading to a spectral resolution of 3 cm^{-1}. The effective dark noise was less than $(1\times10^{-4}$ count/sec)/channel. The multichannel Raman apparatus was essential in obtaining signals, because of the low signal intensity of $CuInSe_2$, which has the large absorption coefficient and allows the incident light to penetrate only in the order of 100 nm in depth. The signal was normally accumulated for 3–12 h. The incident laser power was kept every time below 50 mW at room temperature and below 100 mW at low temperature, respectively, to avoid the damage of the samples. However, the surface temperature increased in vacuum by the laser irradiation. The true temperature was estimated as 100 K from the shift of the Γ_1 mode, which was measured by the incident laser power below 5 mW to avoid the heating. High-pressure experiments were performed by using a diamond window cell at room temperature.[20] The pressure medium was a four-to-one mixture of methanol and ethanol. Pressures were determined from the redshift of the ruby R-line luminescence.[21]

IV. EXPERIMENTAL RESULTS AND DISCUSSION

It is known that many ternary chalcopyrite-structure compounds do not obey clear selection rules.[17] Especially in our experiments, the incident laser energy is much higher than the band-gap energy at about 1 eV. The resonance effect may break the selection rules. This makes the analysis of Raman spectra difficult, and we must be careful in mode assignments when comparing the infrared data or data of analogous compounds such as $AgGaSe_2$.

Figure 2 shows the Raman data of the Γ_1 mode in the $X(Z,Z)\bar{X}$ configuration. The frequencies of the $\Gamma_1^{(1)}[W_1]$ mode are 175 cm^{-1} at room temperature and 178 cm^{-1} at 100 K, respectively. These values are much different from the previous value of 186 cm^{-1} by Gan *et al.*[1]

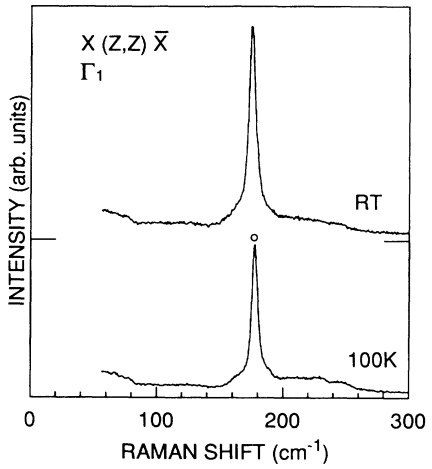

FIG. 2. Raman spectra in the $X(Z,Z)\bar{X}$ configuration.

Figure 3 shows the Raman data in the $Z(Y',X')\bar{Z}$ configuration. Three Γ_3 modes are identified at 100 K. The frequencies of the $\Gamma_3^{(5)}[W_{2l}]$, $\Gamma_3^{(4)}[X_3]$, and $\Gamma_3^{(6)}[W_{2u}]$ modes at 100 K are 67, 179, and 229 cm^{-1}, respectively.

Figure 4 shows the Raman data in (a) the $Z(X,Y)\bar{Z}$ configuration which selects Γ_4 (LO) modes, and (b) the $X'(Y',Y')\bar{X}'$ configuration, which selects Γ_1 and Γ_4 (TO) modes. Figure 5 shows the Raman data in (a) the $X(Z,Y)\bar{X}$ configuration, which selects Γ_5 (LO) modes, and (b) the $X'(Y',Z)\bar{X}'$ configuration, which selects Γ_5 (TO) modes. In all figures, the Γ_1 mode is rather strongly observed, breaking the selection rule, and also some Γ_3 modes are found. The peak at 233 cm^{-1} in Fig. 4(a) and the peak at 217 cm^{-1} in Fig. 4(b) at 100 K are assigned to the LO and TO modes of $\Gamma_4^{(7)}[\Gamma_{15}]$, respectively. These values are mostly in agreement with those of infrared data at room temperature of 231–233 and 212–214

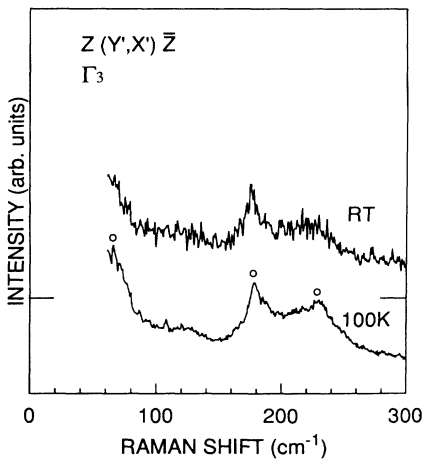

FIG. 3. Raman spectra in the $Z(Y',X')\bar{Z}$ configuration.

cm^{-1}, respectively. The peak at 233 cm^{-1} in Fig. 5(a) and the peak at 217 cm^{-1} in Fig. 5(b) at 100 K are assigned to the LO and TO modes of $\Gamma_5^{(10,16)}[\Gamma_{15}]$, respectively. These values are also mostly in agreement with those of infrared data at room temperature of 229–230 cm^{-1} and 213–215 cm^{-1}, respectively. The Raman frequencies at 100 K of $\Gamma_4^{(7)}[\Gamma_{15}]$ and $\Gamma_5^{(10,16)}[\Gamma_{15}]$ are completely the same with each other, in contrast to the infrared data at room temperature.

All the $1\Gamma_4$ and $2\Gamma_5$ modes originated from the TA branch of the ZB-structure materials are found at less than 80 cm^{-1}. The LO and TO frequencies of the $\Gamma_5^{(11,17)}[X_{5l}]$ mode are 60 and 61 cm^{-1}, those of the $\Gamma_4^{(8)}[W_{2l}]$ mode are 72 and 70 cm^{-1}, and those of the $\Gamma_5^{(14,20)}[W_{4l}]$ mode are 78 and 78 cm^{-1}, at 100 K, respectively. They are in the expected order as mentioned above, except that the frequencies of the LO and TO frequencies of the $\Gamma_5^{(11,17)}[X_{5l}]$ mode are inverted.

The LO and TO frequencies of the $\Gamma_5^{(13,19)}[W_3]$ mode originated from the LA branch are 188 and 188 cm^{-1} at 100 K, respectively. The LO frequency of the $\Gamma_4^{(9)}[W_{2u}]$ mode originated from the TO branch is 200 cm^{-1}. Because of the large intensity of the Γ_1 mode, it is difficult to find its TO frequency. Since the peak frequency of the Γ_1 mode is not 178, but 177 cm^{-1} in Fig. 4(b), we assume that this mode is at the lower tail of the Γ_1 mode, and the frequency is about 177 cm^{-1}. Finally, the LO and TO frequencies of the $\Gamma_5^{(12,18)}[X_{5u}]$ and $\Gamma_5^{(15,21)}[W_{4u}]$ modes originated from the TO branch are assigned as 216, 211, 230, and 227 cm^{-1} at 100 K, respectively. Interestingly, the LO and TO frequencies of the $\Gamma_5^{(15,21)}[W_{4u}]$ mode are buried between those of the $\Gamma_5^{(10,16)}[\Gamma_{15}]$ mode. This is also true for the $\Gamma_3^{(6)}[W_{2u}]$ mode.

Table III and Fig. 6 summarize our results compared to the previous Raman and infrared experiments. The Raman data by Gan *et al.* are completely different from ours.[1] The infrared results are slightly different from each other, even though they are reported by the same

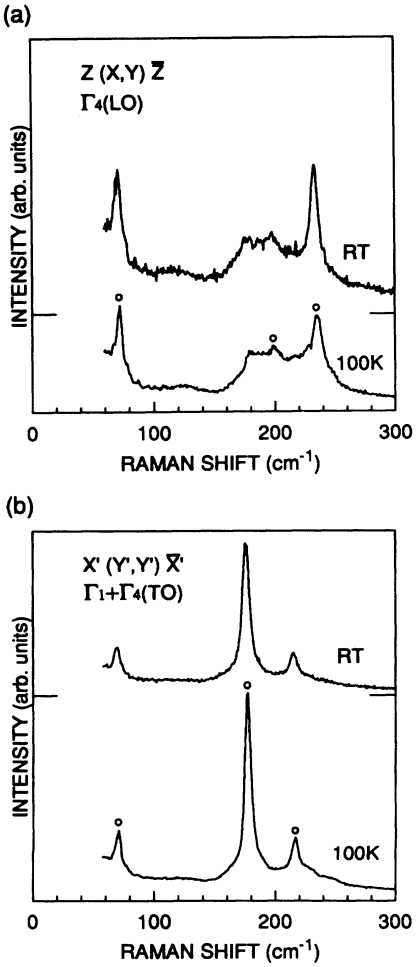

FIG. 4. Raman spectra in (a) the $Z(X,Y)\bar{Z}$ configuration, and (b) the $X'(Y',Y')\bar{X}'$ configuration.

TABLE III. Comparison of the present experimental results with previous infrared-absorption results.

Mode		ir[a]	ir[b]	ir[c]	Raman[d] (RT)[e]	Raman[d] (100 K)
$\Gamma_4^{(7)}[\Gamma_{15}]$	(L)	231	233	232	233	233
	(T)	212	213	214	215	217
$\Gamma_5^{(10,16)}[\Gamma_{15}]$	(L)	229	230	229	230	233
	(T)	215	213	213	217	217
$\Gamma_5^{(15,21)}[W_{4u}]$	(L)					230
	(T)					227
$\Gamma_3^{(6)}[W_{2u}]$						229
$\Gamma_5^{(12,18)}[X_{5u}]$	(L)	212	212	212		216
	(T)	206	206	207	211	211
$\Gamma_4^{(9)}[W_{2u}]$	(L)	195	195	193	198	200
	(T)	169	179	181		177
$\Gamma_5^{(13,19)}[W_3]$	(L)	184	182	183		188
	(T)	167	178	179		188
$\Gamma_3^{(4)}[X_3]$						179
$\Gamma_1^{(1)}[W_1]$					176	178
$\Gamma_5^{(14,20)}[W_{4l}]$	(L)				77	78
	(T)				77	78
$\Gamma_4^{(8)}[W_{2l}]$	(L)	66	64.8	65	71	72
	(T)	63	64	64	70	70
$\Gamma_3^{(5)}[W_{2l}]$						67
$\Gamma_5^{(11,17)}[X_{5l}]$	(L)	67			60	60
	(T)	64			58	61

[a]Reference 2.
[b]Reference 3.
[c]Reference 4.
[d]Our data.
[e]Room temperature.

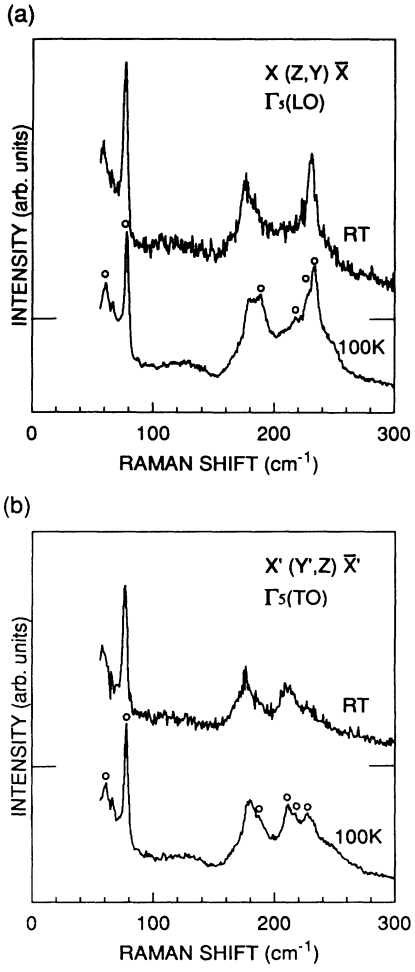

FIG. 5. Raman spectra in (a) the $X(Z,Y)\bar{X}$ configuration, and (b) the $X'(Y',Z)\bar{X}'$ configuration.

TABLE IV. The frequencies of the Γ_1 mode ω_0, the linear pressure coefficients b, and the mode Grüneisen coefficients at room temperature γ_{Γ_1} of $CuInSe_2$ and related ternary compounds.

	ω_0 (cm^{-1})	b (cm^{-1}/GPa)	B_T (GPa)	γ_{Γ_1}
$CuInSe_2$[a]	173	5.0	43.5[b]	1.3
$CuAlS_2$[c]	315	5.4	94.0	1.6
$CuGaS_2$[c]	312	6.0	94.0	1.8
$CuGaS_2$[d]	312	4.8	94.0	1.5
$AgGaS_2$[d]	293	5.0	60.0	1.02
$CdSiP_2$[e]	323	5.5	97.0	1.65

[a]This work.
[b]Reference 22.
[c]Reference 23.
[d]Reference 24.
[e]Reference 25.

group.[2–4] Our data of the Γ_4 and Γ_5 modes are mostly in good agreement with theirs. Gan *et al.* also measured the Raman spectra of the solid solution $(CuInSe)_{1-x}$-$(2ZnSe)_x$.[1] They found a sudden dip of the frequencies when x changes from 0 to 0.08. This extraordinary dip does not exist in our data and the infrared data.

As Camassel, Artus, and Pascual discussed,[14] the optical-phonon modes of $AgGaSe_2$ are grouped into three energy bands: high-frequency region around 250 cm^{-1}, intermediate region in the range 135–180 cm^{-1}, and low-frequency region in the range 25–85 cm^{-1}. This feature is not reproduced in $CuInSe_2$. Since the frequencies of the $\Gamma_4^{(7)}[\Gamma_{15}]$ and $\Gamma_5^{(10,16)}[\Gamma_{15}]$ modes of $CuInSe_2$, which are dominated by the motion of the In atoms, are much smaller than those of $AgGaSe_2$, the high-frequency region and the intermediate region are in the same energy

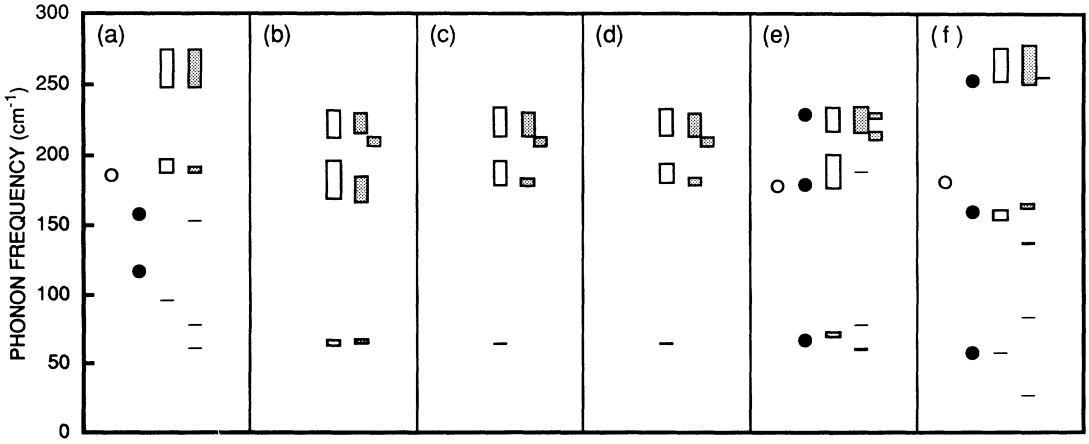

FIG. 6. Summary of the observed phonon frequencies. Open circles, closed circles, open squares, and hatched squares show the Γ_1, Γ_3, Γ_4, and Γ_5 modes, respectively. The upper and lower sides of the squares represent the frequencies of the LO and TO modes, respectively. (a) Raman data by Gan *et al.* (Ref. 1), (b) infrared data by Riede *et al.* (Ref. 2), (c) infrared data by Neumann *et al.* (Ref. 3), (d) infrared data by Neumann (Ref. 4), (e) our Raman data, and (f) infrared and Raman data of $AgGaSe_2$ by Camassel, Artus, and Pascual (Ref. 14). Only our data are taken at 100 K, and all the others are at room temperature.

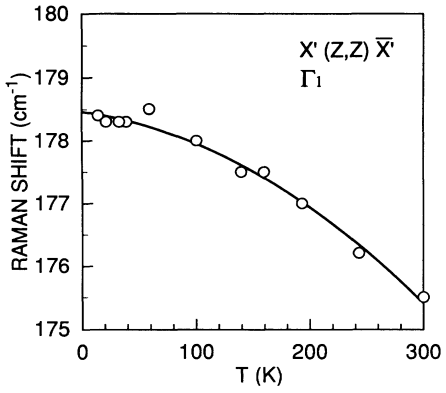

FIG. 7. Temperature dependence of the peak frequency of the Γ_1 mode. The solid line is only a guide to the eye.

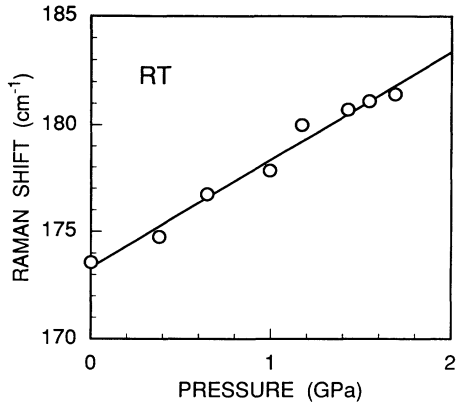

FIG. 8. Pressure dependence of the peak frequency of the Γ_1 mode at room temperature. The solid line corresponds to the result of a least-squares fit to the experimental data using a linear equation.

range for $CuInSe_2$. Hence, we find a more complicated energy mixing among the modes with the Γ_4 and Γ_5 symmetries and quite different energy ordering of the Γ_5 modes as seen in Fig. 6. Another big difference between $CuInSe_2$ and $AgGaSe_2$ is that the LO-TO splitting of the $\Gamma_4^{(9)}[W_{2u}]$ mode is very large in $CuInSe_2$, but not as large in $AgGaSe_2$. On the contrary, the LO-TO splittings of the $\Gamma_4^{(7)}[\Gamma_{15}]$ and $\Gamma_5^{(10,16)}[\Gamma_{15}]$ modes of $CuInSe_2$ are smaller than those of $AgGaSe_2$.

V. TEMPERATURE AND PRESSURE EFFECTS

Figure 7 shows the temperature dependence of the peak frequency of the Γ_1 mode. By increasing temperature, the frequency is almost constant below 50 K and begins to decrease linearly from around 50 K. The crystal may become harder at low temperature. The twisting motion of the tetrahedron of the Se atoms, which creates the Γ_1 phonon mode, will be more difficult at low temperature because of the higher rigidity of the Cu and In sublattices.

Figure 8 shows the pressure dependence of the peak frequency of the Γ_1 mode at room temperature. Only the Γ_1 mode could be resolved under pressure by using the diamond window cell, because the luminescence of the diamonds overlaps the Raman signal. The solid line in Fig. 8 corresponds to the results of at least-squares fit of a linear relation $\omega=\omega_0+bP$ to the experimental data. The frequency at ambient pressure ω_0 of 173 cm^{-1} is slightly lower than 175 cm^{-1} of Fig. 2. This may reflect the difference of the microscopic characteristics of the sample crystals, since here we used a sample from a different ingot. The peak frequency increases linearly up to 2 GPa, with the linear coefficient b of 5.0 cm^{-1}/GPa. Since bulk modulus B_T was given by 43.5 GPa, we calculate the mode Grüneisen parameter γ_{Γ_1} to be 1.3. In Table IV we summarize our data compared to the reported values of the other chalcopyrite-structure compounds. The obtained value of the mode Grüneisen constant is mostly the same as those of the other compounds.

VI. EFFECTIVE CHARGES

The magnitude of the LO-TO splitting is determined by the macroscopic effective charges. Following the formalization by Scott, we can estimate the effective charges easily.[26,27] In the rigid-ion approximation, there is a relationship between the splittings and the effective charges:

$$\pi V\frac{c^2 m}{e^2}\sum_{j(\Gamma_4,\Gamma_5)}(\nu_{\mathrm{LO}_j}^2-\nu_{\mathrm{TO}_j}^2)=\frac{2(Z_A^*)^2}{m_A}+\frac{2(Z_B^*)^2}{m_B}+\frac{4(Z_C^*)^2}{m_C},$$

where j sums over the $3\Gamma_4$ and $6\Gamma_5$ modes; V is the volume of the unit cell, and m is the atomic mass unit. m_A, m_B, and m_C are the atomic masses, and Z_A^*, Z_B^*, and Z_C^* are the effective charges of atom A^{I} (Cu), B^{III} (In), and C^{VI} (Se), respectively. Another relation is given by the expression of the lattice neutrality:

$$2Z_A^*+2Z_B^*+4Z_C^*=0\ .$$

A reasonable value for Z_C^* (Z_{Se}^*) will be -0.865, which is estimated as the averaged value of -0.83 and -0.9 of two binary compounds ZnSe and CdSe, respectively.[12,27] Then from the above two equations, we get Z_A^* (Z_{Cu}^*)$=0.475$ and Z_B^* (Z_{In}^*)$=1.255$.

This means that the electronic contribution to the LO-TO splitting of the zone-center modes of the A (Cu) atom is 38% of the B (In) atom, which must be 33%, if we consider only the valence electrons neglecting the charge transfer. If we assume the repartition of the valence charges e^* is proportional to the repartition of the effective charges, we get e_A^* (e_{Cu}^*)$=1.10$ and e_B^* (e_{In}^*)$=2.90$. These sums indicate that only 0.05 electrons per bond had to be transferred from the In atoms to the Cu atoms through the common anions, in order to screen the point-ion perturbation from the ZB charge distribution. The situation is very different from the analog compound $AgGaSe_2$, which has Z_A^* (Z_{Ag}^*)$=0.67$, Z_B^*

$(Z^*_{Ga})=1.03$, e^*_A $(e^*_{Ag})=1.6$, and e^*_B $(e^*_{Ga})=2.40$ and where 0.3 electron per bond is transferred. This difference may be consistent with the fact that the chalcopyrite distortion η is almost 1 in the case of $CuInSe_2$, but is deviated from 1 in the case of $AgGaSe_2$.

VII. CONCLUSION

Performing Raman studies at low temperature, we found all 22 Raman-active zone-center modes of $CuInSe_2$. The results are consistent with the previous reports of infrared studies. The charge transfer between Cu and In of $CuInSe_2$ is estimated to be much less than that of $AgGaSe_2$.

ACKNOWLEDGMENTS

This work was supported by the Sunshine Project of the Agency of Industrial Science and Technology (AIST) of Japan, and by Special Coordination Funds for Promoting Science and Technology of Science and Technology Agency (STA) of Japan (Project of "Elementary Function of Materials"). One of the authors (H.T.) would like to thank H. Okushi, T. Yao, H. Tokumoto, and K. Kajimura for their continuing support and encouragement.

[1]J. N. Gan, J. Tauc, V. G. Lambrecht, and M. Robbins, Phys. Rev. B **13**, 3610 (1976).
[2]V. Riede, H. Sobotta, H. Neumann, H. X. Nguyen, W. Müller, and G. Kühn, Solid State Commun. **28**, 449 (1978).
[3]H. Neumann, R. D. Tomlinson, W. Kissinger, and N. Avgerinos, Phys. Status Solidi B **118**, K51 (1983).
[4]H. Neumann, Solar Cells **16**, 399 (1986).
[5]H. Sobotta, H. Neumann, W. Kissiinger, G. Kühn, and V. Riede, Phys. Status Solidi B **103**, K125 (1982).
[6]S. Yamanaka, M. Konagai, and K. Takahashi, Jpn. J. Appl. Phys. **28**, L1337 (1989).
[7]M. Tanda, S. Yamanaka, N. Nakada, A. Yamada, M. Konagai, and K. Takahashi, *Technical Digest of 5th International Photovoltaic Science and Engineering Conference, Kyoto, 1990* (Showado Insatsu, Japan, 1990), p. 279.
[8]T. Hama, T. Ihara, H. Sato, H. Fujisawa, M. Ohsawa, Y. Ichikawa, and H. Sakai, *Technical Digest of 5th International Photovoltaic Science and Engineering Conference* (Ref. 7), p. 283.
[9]S. Yamanaka, M. Tanda, N. Nakada, A. Yamada, M. Konagai, and K. Takahashi, Jpn. J. Appl. Phys. **30**, 442 (1991).
[10]S. Kohiki, M. Nishitani, T. Negami, K. Nishikura, and T. Hirao, Appl. Phys. Lett. **59**, 1749 (1991).
[11]H. Nakanishi, T. Maeda, S. Ando, E. Endo, T. Irie, H. Tanino, and T. Yao (unpublished).
[12]J. E. Jaffe and A. Zunger, Phys. Rev. B **28**, 5822 (1983).
[13]J. E. Jaffe and A. Zunger, Phys. Rev. B **29**, 1882 (1984).
[14]J. Camassel, L. Artus, and J. Pascual, Phys. Rev. B **41**, 5717 (1990).
[15]L. Artus, J. Pujol, J. Pascual and J. Camassel, Phys. Rev. B **41**, 5727 (1990).
[16]H. W. Spiess, V. Haeberln, G. Brandt, A. Rauber, and J. Schneider, Phys. Status Solidi B **62**, 183 (1974).
[17]G. D. Holah, J. S. Webb, and H. Montgomery, J. Phys. C **7**, 3875 (1974).
[18]A. Miller, A. Mackinnon, and D. Weaire, in *Solid State Physics*, edited by F. Seitz and D. Turnbull (Academic, New York, 1981), Vol. 36, p. 199.
[19]H. Tanino, and H. Okuskhi, Jpn. J. Appl. Phys. **29**, L2133 (1990).
[20]H. Tanino, Rev. Sci. Instrum. **57**, 2992 (1986).
[21]G. J. Piermarini, S. Block, J. D. Barnett, and R. A. Forman, J. Appl. Phys. **46**, 2774 (1975).
[22]K. J. Bachmann, F. S. L. Hau, F. A. Thiel, and H. M. Kasper, J. Electron. Mat. **6**, 431 (1977).
[23]M. Bettini and W. B. Holzapfel, Solid State Commun. **16**, 27 (1975).
[24]C. Carlone, D. Olego, A. Jayaraman, and M. Cardona, Phys. Rev. B **22**, 3877 (1980).
[25]S. Shirakata, Jpn. J. Appl. Phys. **27**, 2113 (1988).
[26]J. F. Scott, Phys. Rev. B **4**, 1360 (1971).
[27]H. A. Lauwers, J. Phys. Chem. Solids **49**, 173 (1988).

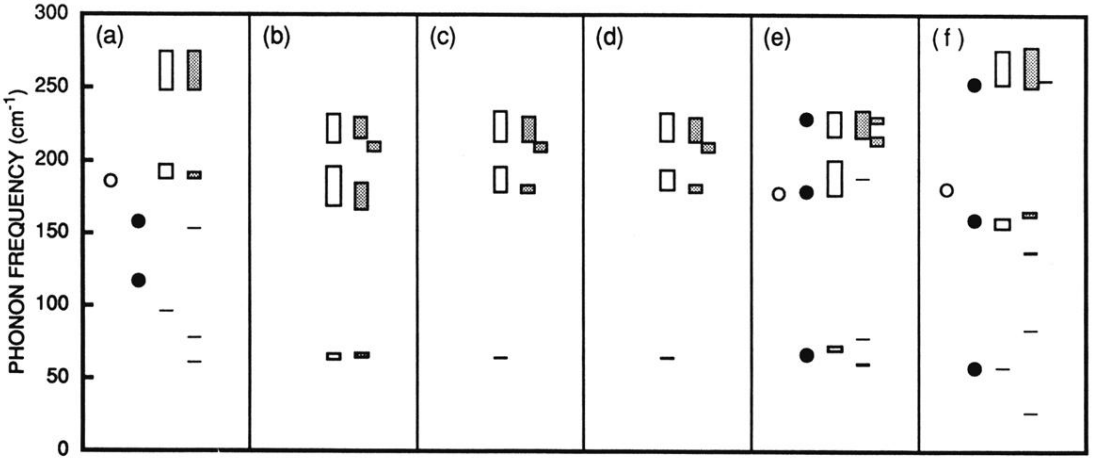

FIG. 6. Summary of the observed phonon frequencies. Open circles, closed circles, open squares, and hatched squares show the Γ_1, Γ_3, Γ_4, and Γ_5 modes, respectively. The upper and lower sides of the squares represent the frequencies of the LO and TO modes, respectively. (a) Raman data by Gan *et al.* (Ref. 1), (b) infrared data by Riede *et al.* (Ref. 2), (c) infrared data by Neumann *et al.* (Ref. 3), (d) infrared data by Neumann (Ref. 4), (e) our Raman data, and (f) infrared and Raman data of $AgGaSe_2$ by Camassel, Artus, and Pascual (Ref. 14). Only our data are taken at 100 K, and all the others are at room temperature.